Supporting Information for

Crystalline Arrays of Pairs of Molecular Rotors: Correlated Motion, Rotational Barriers, and Space Inversion-symmetry Breaking due to Conformational Mutations

Cyprien Lemouchi,[†] Konstantinos Iliopoulos,[†] Leokadiya Zorina,[†,#] Sergey Simonov,[†,#] Pawel Wzietek,[¶] Thomas Cauchy,[†] Antonio Rodríguez-Fortea,[‖] Enric Canadell,[§] Jiři Kaleta,[‡] Josef Michl,[‡,⊥] Denis Gindre,[†] Michael Chrysos[†] and Patrick Batail*[,†]

This PDF file includes:

Characterization of 1, 2 and 4.

Computational details and results

Calculations for BCO and 1,4-Bis(4-ethynyl)bicyclo[2,2,2]oct-1-yl)buta-1,3-diyne

Vibrational frequencies and energy difference associated with the different local environments of the rotor

Rotational barriers

Car-Parrinello molecular dynamics

Second harmonic generation experiments

Figures S1 to S15
Table S1

References (37-42)

Characterization of bis((4-(4-pyridyl)-ethynyl)bicyclo[2.2.2]octan-1-yl)buta-1,3-diyne, 1. ^{1}H-NMR (300 MHz, $CDCl_3$): δ 8.5 (d, 4.5 Hz, 4H), 7.3 (d, 4.5 Hz, 4H), 1.8 (s(*broad*), 24H); ^{13}C-NMR (300MHz, $CDCl_3$) δ 148.1, 133.8, 126.4, 103.3, 84.35, 78.6, 65.4, 31.3, 27.1-27.0; Maldi-Tof(mode +) (m/z) : calcd for $C_{34}H_{33}N_2^+$, 469.3; found, 469.3.

Characterization of 1,4-bis(4'-pyridylethynyl)bicyclo[2.2.2]octane, 2. ^{1}H-NMR (300 MHz, $CDCl_3$): δ 8.5 (dd, J = 1.5 Hz, 4.5 Hz, 4H), 7.2 (dd, J = 1,5 Hz, 4.5 Hz, 4H), 1.9 (s, 12H); ^{13}C-NMR (300MHz, $CDCl_3$) δ 149.7, 132.1, 125.9, 101.4, 78.8, 31.5, 27.0; ESI(+) (m/z) : calcd for $C_{22}H_{21}N_2^+$, 313.2; found, 313.2; Analysis (calcd, found for $C_{22}H_{20}N_2$): C (84.58, 84.32), (H 6.45, 6.57), (N 8.97, 8.66). (Degradation temp. 202 °C)

Synthesis of 1,4-bis(3-((trimethylsilyl)ethynyl)bicyclo[1.1.1]pent-1-yl)buta-1,3-diyne, 4. All reactions were carried out under argon atmosphere with dry solvents, freshly distilled under anhydrous conditions, unless otherwise noted. Standard Schlenk and vacuum line techniques were employed for all manipulations of air- or moisture-sensitive compounds. Yields refer to isolated, chromatographically and spectroscopically homogeneous materials, unless otherwise stated. Ethyl 2-bromoacetate, $PdCl_2(PPh_3)_2$ and CuI were purchased and used without further purification. THF was distilled from sodium and benzophenone under argon immediately prior to use. Triethylamine was distilled from CaH_2 under argon prior to use. Melting point was determined with a standard apparatus and is uncorrected. ^{1}H and ^{13}C spectra were acquired at 25 °C 400 MHz spectrometer. ^{1}H and ^{13}C spectra were referenced to residual solvent peaks. GC-MS were measured on an instrument with a fused silica capillary column (cross-linked 5% phenyl methyl silicone).

Characterization of 1,4-Bis(3-((trimethylsilyl)ethynyl)bicyclo[1.1.1]pent-1-yl)buta-1,3-diyne, 4. Mp > 230 °C (dec.). ^{1}H NMR (400 MHz, $CDCl_3$): δ 0.13 (s, 18H, CH_3), 2.30 (s, 12H, CH_2). ^{13}C NMR (100 MHz, $CDCl_3$): δ 0.1, 30.2, 30.9, 59.2, 64.7, 77.5, 85.0, 104.3. IR (KBr): 2994, 2966, 2916, 2879, 2162, 1448, 1410, 1317, 1261, 1253, 1242, 1233, 1095, 916, 857, 845, 759, 724, 698, 622 cm^{-1}. MS, *m/z* (%): 374.2 (M, 6), 359.2 (M – CH_3, 24), 343.1 (8), 329.1 (11), 315.1 (9), 301.1 (M – TMS, 14), 285.1 (26), 271.1 (29), 257.1 (18), 243.1 (10), 233.1 (9), 202.1 (11), 179.0 (7), 155.1 (8), 107.0 (12), 97.0 (23), 83.0 (13), 73.0 (TMS, 100), 67.0 (7), 59.0 (14), 45.0 (11). HRMS, (APCI) for ($C_{24}H_{30}Si_2$ + H^+): calcd 375.19588, found 375.19553. Anal. Calcd for $C_{24}H_{30}Si_2$: C, 76.94; H, 8.07. Found: C, 76.68; H, 8.10.

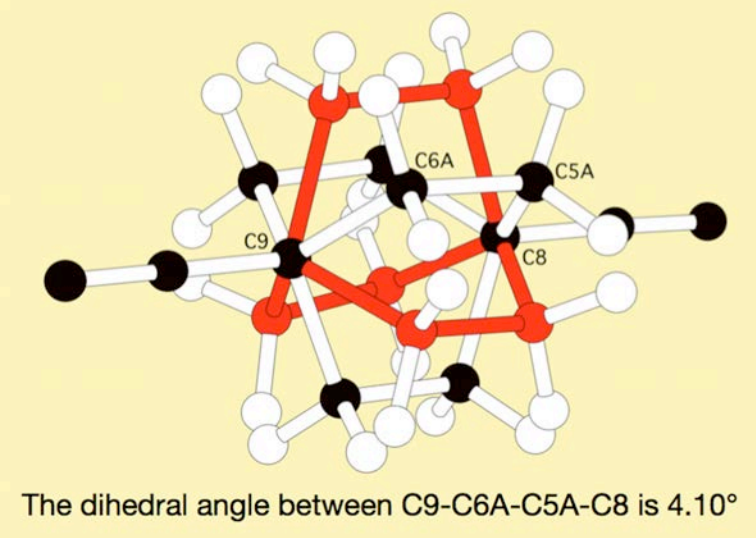

Figure S1. Example of one dihedral angle (see Scheme 7). Here are displayed the rotors disordered on two sites in the 295 K structure where the white blades are for the 88% occupancy position and the red blades for the 12% occupancy position.

Computational details and results.

Calculations for BCO and 1,4-Bis(4-ethynyl)bicyclo[2,2,2]oct-1-yl)buta-1,3-diyne. The geometry and electronic structure of the different minima and transition states were computed by density functional theory (DFT).[20] An hybrid version of the PBE functional[37] usually referred as PBE0[38] as implemented in the Gaussian09 package[23] has been used with an extended triple-ζ basis set.[39] Susceptibility tensors were evaluated by a perturbative Coupled Perturbed Hartree-Fock based method, static and dynamic. The topologies calculated for the frontier orbitals was analysed for both BCO and 1,4-Bis(ylethynyl)bicyclo[2.2.2]octane-1-yl)buta-1,3-diyne, a model fragment for **1**. They are similar to earlier descriptions[10] and likewise suggest a good periplanar overlap of the π orbitals of the alkynes with the σ bonds originating at the bridgehead of the bicyclo[2.2.2]octane propellers. Hence, a dominant communication conduit would be the set of three σ-bonds oriented essentially parallel to the π-conjugated ethynyl manifold. The degenerate HOMO and HOMO-1 for **1** are localized (Figure S2) on the inner diethynyl core of the molecule and, likewise, their calculated topologies demonstrate the occurrence of a similar communication channel involving a symmetrical set of propellers' three σ-bonds with the π-conjugated ethynyl manifold properly connecting the two rotator units within the molecule.

The most stable calculated configuration is anyone of the two staggered, chiral D_3 conformations (Scheme 7) yet, neither an eclipsed, D_{3h} conformation, calculated to be 127 cal mole^{-1} less favourable in energy, nor any angle between the two three-bladed propellers, will severe the communication between the latter or between the π system and the propellers. Hence, the communication between the σ- and π-manifolds is expected to be sustained at room temperature upon quantum rotations of the helix blades between the two D_3 configurations of the two bicyclo[2.2.2]octane rotators in **1**. With materials applications in mind, we recognized that this hybrid σ/π conduit would enhance the anisotropy of the molecular polarizability tensor. With the *z* axis set along the gyroscope axle, the calculated polarizability tensor components are $\alpha_{xx} = \alpha_{yy} = 107$,

α_{zz} = 181 for BCO and α_{xx} = α_{yy} = 203, α_{zz} = 490 for **1** regardless of the bicyclo[2.2.2]octane configuration. Finally, the first electronic transitions were simulated by a linear response method (Time Dependent Density functional Theory (TD-DFT)) with the same functional and basis set as the CPHF and DFT calculations. The first electronic transitions calculated by TD-DFT, be they singlet-singlet or singlet-triplet, occurs at 187 nm for BCO and 263 nm for **1**, demonstrating that no electronic transition occurs at the wavelength of the SHG experiment; note that none is indeed identified in the electronic absorption spectra recorded on crystals of **1** (Figure S12). Therefore, no resonant process is anticipated upon excitation.

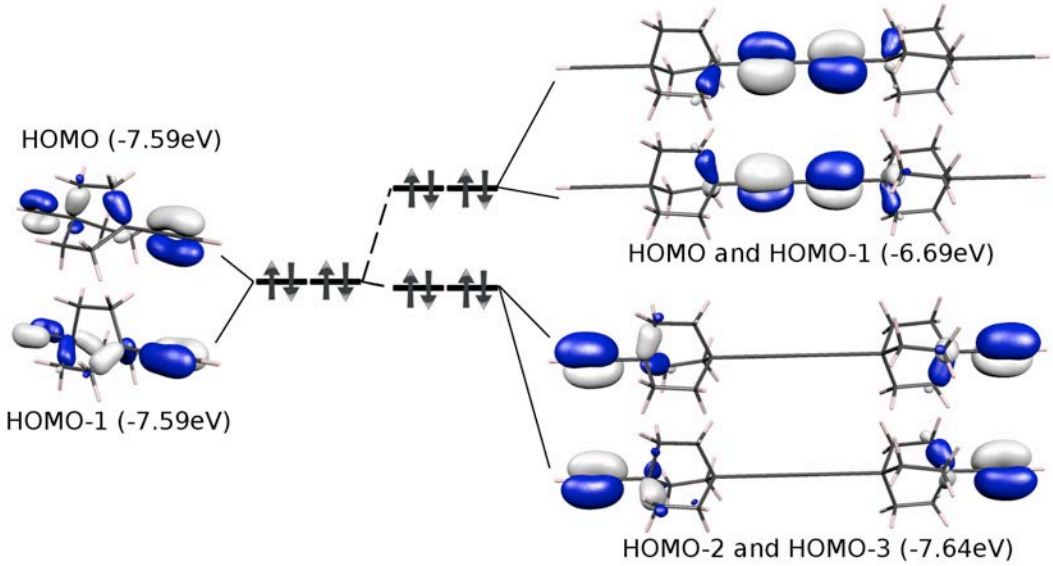

Figure S2. Relationship between the frontier orbitals of BCO and 1,4-bis(4-ethynyl)bicyclo[2.2.2]oct-1-yl)buta-1,3-diyne, a model fragment for **1**. Because of the three-fold axis there are always two degenerate e orbitals allowing for a good mixing regardless of the relative propellers' orientation. Hence, the barrier to the rotation is very small and the movement of the rotors is essentially frictionless, i.e., there is no energy dissipation.

Vibrational frequencies and energy difference associated with the different local environments of the rotor. Calculation of the harmonic vibrational frequencies for isolated **1** and for the reduced model in which the pyridines were substituted by hydrogen atoms were carried out using the hybrid M06-2X functional[21] and the 6-31G(d,p) basis set[22] as implemented in the Gaussian09 package.[23] The lowest frequency, with a very small value of 8 cm^{-1} for the model system with hydrogens and 11 cm^{-1} for **1**, corresponds to a normal mode of vibration in which the two rotors are rotating out-of-phase (see Figure S3) and there are no other relatively low frequency normal modes corresponding to internal rotations.

In order to evaluate the energy difference associated with the different local environments of the rotor, we carried out DFT calculations for a model in which one of the two rotors of **1** was in the presence of all other neighbouring rotor units making H···H contacts shorter than 2.8 Å. We considered the contacts out of one of the two rotors. We also considered all the pyridine units associated with N···H hydrogen bonds. Because of the very large number of atoms involved and the local nature of the interactions we used a full central molecule **1** and appropriate fragments of **1** including

the rotor or pyridine units. Thus the full model (see Figure S4) contains one molecule **1**, two 4-((4-ethynylbicyclo[2.2.2]oct-1-yl)ethynyl)pyridine, three 1,4-(pyridine-4-ylethynyl)bicyclo[2.2.2]oct, one bicyclo[2.2.2]octane and one pyridine, i.e. a total of 314 atoms. The calculations used the crystal geometries at the above mentioned M06-2X/6-31G(d,p) level (more than 3000 basis functions). The interaction energies per rotor were calculated as the energy difference between the full system and that of the different components. When all the neighbouring rotor units exhibit the majority equilibrium position (88% occupancy) the difference in interaction energies between the cases in which the central rotor unit of **1** under consideration is either in the majority or minority equilibrium position, is 1.2 kcal mol^{-1}. When all the neighbouring rotor units exhibit the minority equilibrium position (12% occupation), this value is 5.5 kcal mol^{-1}. Remarkably, this large energy difference is associated with one of the interactions between neighbouring units exhibiting both the minority equilibrium conformation leading to H···H distances shorter than 2.4 Å (2.103, 2.225, 2.241, 2.278 Å). Other interactions associated with combinations of majority and/or minority equilibrium conformations, lead to rotor-rotor H···H distances larger than 2.4 Å. In all these cases the interaction energy differences are small (<1.5 kcal mol^{-1}). However, when all neighbouring rotors are in the majority equilibrium conformation except those leading to the above mentioned rotor-rotors H···H contacts shorter than 2.40 Å, having the minority equilibrium position in the central molecule **1** disfavours the system by 5.0 kcal mol^{-1}. Therefore, it is clear that those rotor-rotor H···H contacts shorter than 2.4 Å occurring between neighbouring equilibrium positions with 12% occupancy penalize the system by an energy which matches very well the difference in activation energies obtained in the ^{1}H T_1 spin-lattice relaxation experiments.

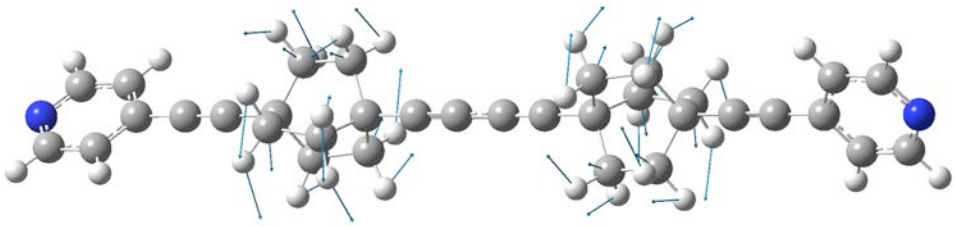

(a)

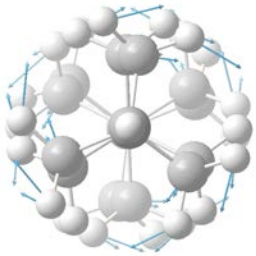

(b)

Figure S3. The blue arrows represent the normal mode of vibration (NMV) corresponding to the internal out-of-phase rotation of one rotor with respect to the other. (a) Side view; (b) View along the rotor axle.

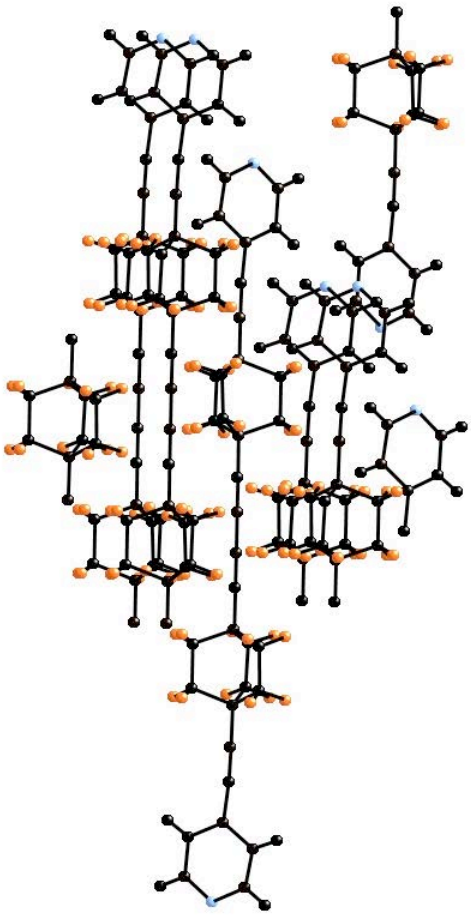

Figure S4. Structural model used in the DFT calculations to estimate the energy difference associated with the different local environments of one rotor (the hydrogen atoms of the rotor units are shown in orange and the pyridine nitrogen atoms in blue).

Rotational barriers. The estimations of the energy barriers for the rotation of two adjacent double-rotors gears done from the energy minima of the two different crystallographic sites (88/12) lead to the conclusion that the low-energy barrier (1 kcal mol^{-1}) corresponds to the correlated synchronous motion of the rotors whereas the higher-energy barrier (around 5-6 kcal mol^{-1}) is due to their correlated asynchronous motion. Besides these estimations, computed from energy differences between different crystal structures (majority and minority positions), we have also estimated the two rotation barriers for synchronous and asynchronous motion searching for the lowest-energy path by means of partial geometry optimizations. We have used a model with two adjacent rotors that have been capped at the two sides in the following manner: 1) by a -C≡CH group on one side; 2) by a H_2C- simulating the sp^2 C of the pyridine on the other (see Figure S5). For the synchronous motion, we have fixed the dihedral angle C(blade)-C(rotor)-C(terminal group)-H (atom numbers 12, 20, 10 and 54, respectively, in Figure S6) for one rotor as well as the positions of atoms H_2C-C- (54, 53, 10, 14; Fig. 2) on one side and -CH (25 and 49, Figure S6) on the other. The coordinates of the adjacent rotor have been fully optimized, except atoms H_2C-C- (51, 50, 9, 13; Figure

S6) on one side and -CH (26 and 52, Figure S6) on the other, which kept the crystallographic positions.

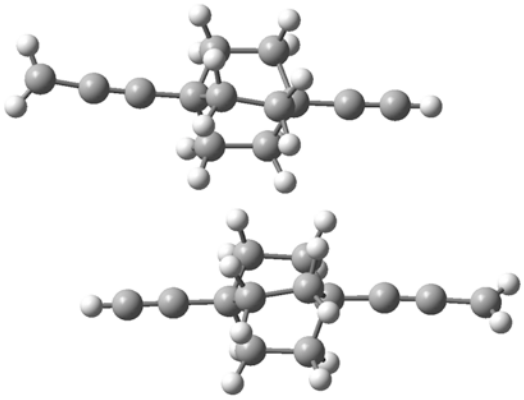

Figure S5. Model to study the correlated motion between two adjacent rotors.

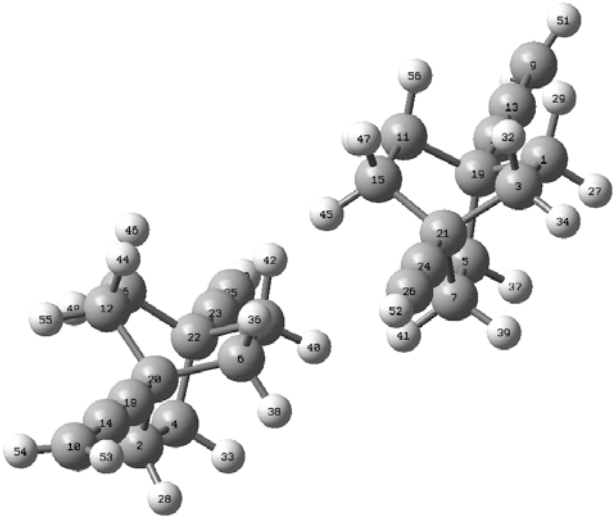

Figure S6. Model to study the correlated motion between two adjacent rotors with the atoms correspondingly numbered. Terminal H_2C-C- and -CH groups of the two rotors are always fixed (atoms 54, 53, 10, 14; 25, 49; 51, 50, 9, 13; 26, 52). For the synchronous motion, we fix the 54-10-20-12 dihedral angle and change it every 10 degrees. For the asynchronous motion, we also fix the 51-9-19-11 dihedral at the same value as the 54-10-20-12 angle. Theta = 0 corresponds to the dihedral angle of the crystal structure.

Figure S7 shows the structures at two points (theta = 40 degrees) for the synchronous and asynchronous motions. The results for the barriers computed in this way (see Figure S8) are in excellent agreement with the experimental results and with the previous estimations obtained from the energy minima in the crystallographic sites.

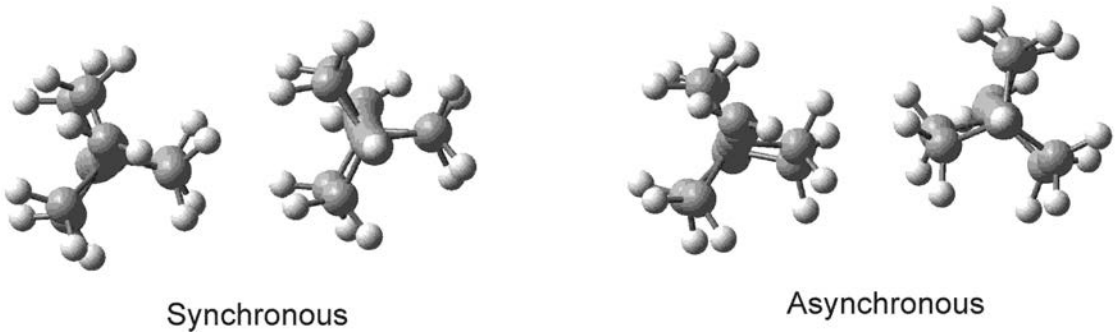

Figure S7. Structures at theta = 40 degrees for the synchronous (left) and asynchronous (right) paths.

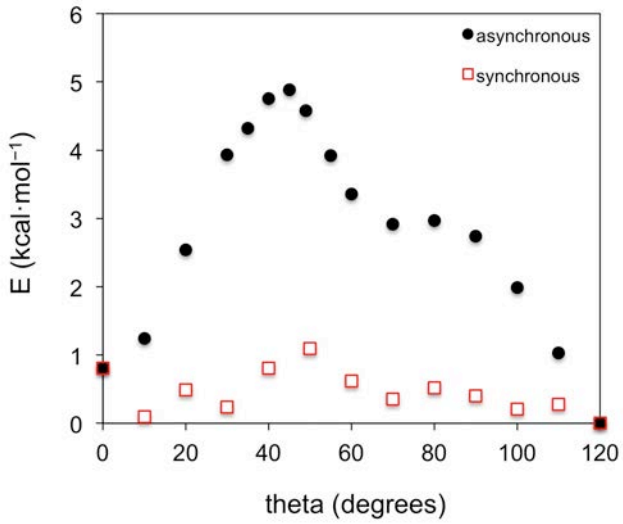

Figure S8. Computed energy profiles (in kcal mol^{-1}) for the synchronous and asynchronous rotation of two adjacent rotors.

Car-Parrinello molecular dynamics. Calculations were carried out for isolated **1** with the terminal pyridines substituted by hydrogen atoms using the CPMD code (see movie double-rotor.wmv).[24,25] The simulations were performed in a cubic box with side lengths of 28 Å. The core electrons are described by Troullier-Martins norm-conserving pseudopotentials.[40] The electronic potential was calculated by means of the PBE density functional[37] using a plane waves basis set with a cutoff of 40 Ry. The time step was set to 0.096 fs and the fictitious electron mass to 600 au. The system was first equilibrated at 300 K using the Nosé-Hoover chain thermostat.[41,42] Production runs of 15 and 38 ps at 300 K were performed. The frequency for the internal rotation of one rotor with respect to the other is estimated to be around 260 MHz. The variation of the dihedral angle C(blade, rotor 1)-C(axis, rotor 1)-C(axis, rotor 2)-C(blade, rotor 2) along the trajectory for the longest simulation (rotational degree of freedom of the rotor, see Chart 2) is plotted in Figure S9a. The change of the dihedral angle within one blade of the rotor C(axis)-C(blade)-C(blade)-C(axis) along the trajectory for the longest simulation (torsional degree of freedom of the rotor, see Chart 2) is plotted in Figure S9b. There are around 70 cycles of dihedral changes (i.e. chirality switches according to Scheme 7)

during the 38 ps simulation (around 550 fs/cycle), in good agreement with the small computed barrier of around 0.1 kcal/mol in the gas phase.
Car-Parrinello simulations were also carried out using a simple system that models the "gear" made by two adjacent double rotors (see movie two-rotors.wmv). The model is the same as that used for the study of the rotational barriers (Figures S5-S6). The six terminal H atoms (54, 53, 49; 50, 51, 52 in Figure S6) were maintained fixed during the dynamics to simulate the relatively fixed position of the double rotor along the rotor axle in the solid state. All the computational settings were the same as in the previous simulations, except the side lengths of the cubic box, which are now 25 Å. The simulation time was 49 ps. Figure S9c shows the rotation of the two rotors, i.e. the change of the H(54)-C(10)-C(20)-C(12) and H(51)-C(9)-C(19)-C(11) dihedral angles according to labels in Figure S6, along the trajectory.

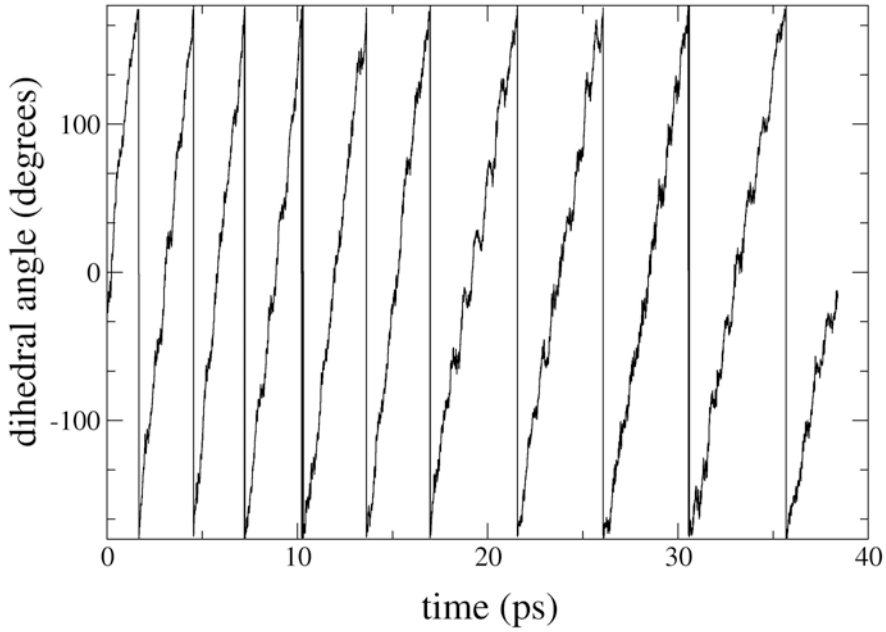

Figure S9a. Plot of the dihedral angle C(blade, rotor 1)-C(axis, rotor 1)-C(axis, rotor 2)-C(blade, rotor 2) along the trajectory for one of the Car-Parrinello molecular dynamics simulations (rotational degree of freedom according to Chart 2).

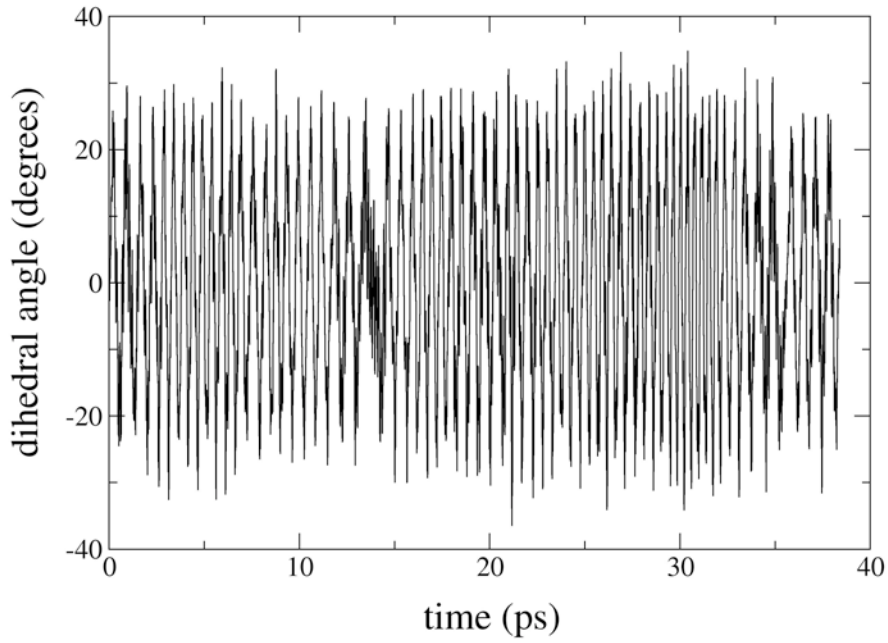

Figure S9b. Plot of the dihedral angle within one blade of the rotor C(axis)-C(blade)-C(blade)-C(axis) along the trajectory for one of the Car-Parrinello molecular dynamics simulations (torsional degree of freedom according to Chart 2, also represented in Scheme 7).

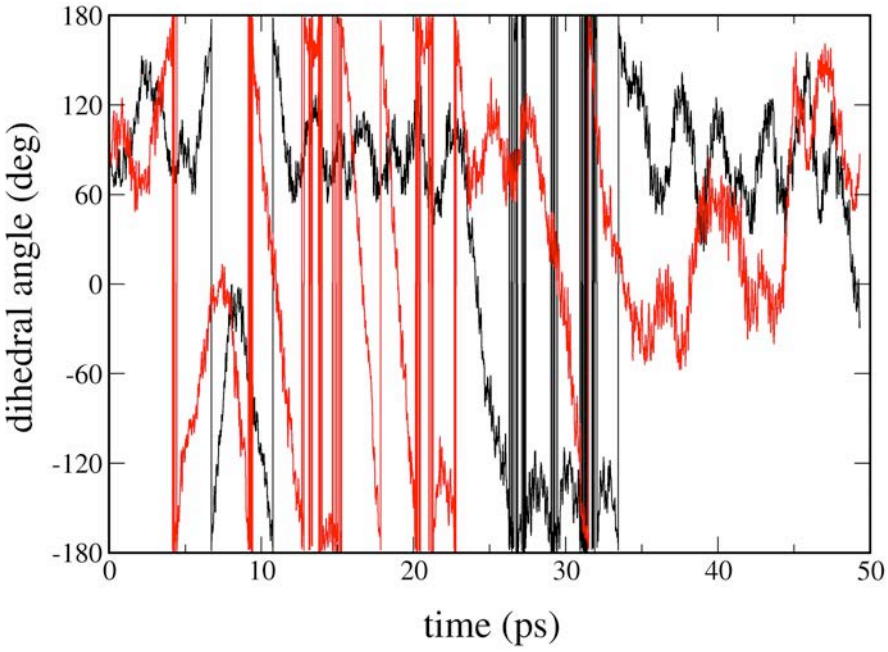

Figure S9c. Plot of the H-C(terminal H_2C-)-C(rotor axis)-C(blade) dihedral angles of the two rotors (black: rotor 1, atoms 54-10-20-12 in Fig. S6; red: rotor 2, atoms 51-9-19-11 in Figure S6).

Second harmonic generation experiments.

Special care and lengthy measurements were performed (Figure S10) in order to reach the ideal experimental conditions, which provide high signal to noise ratio without causing destruction/surface effects to the bulk or the surface of the crystal. The laser power was set to 0.8 mW, while each SHG spectrum was integrated for 7 seconds. Under these conditions the crystal of **1** delivered an intense and stable SHG signal sustained up to two hours of irradiation, demonstrating that no destruction was taking place. Note that in the experiment presented in Figure 4b, the SHG level remains identical at the beginning (δ = -180 degrees) and end of the experiments (δ = +180 degree) verifying that no degradation of the crystal occurred throughout the measurements.

The SHG efficiency was first investigated as a function of the angle between a* and the incident laser beam. The SHG response has been measured for every angle investigated, while the crystal has been repositioned for each angle by the X-Y-Z stage in order to be perfectly focused throughout the rotation. Data in Figure 4 have been obtained by integration of the SHG part of the spectra for each position. A neat signal modulation is recorded upon variation of the incident angle with a maximum at about 30 degrees.

Then, the crystal orientation was set at 30 degrees, the orientation which was previously found to correspond to maximum SHG response. A second series of measurements was then carried out upon changing the direction of the polarization of the laser beam by rotating the λ/2 waveplate. In this way, the intensity of the laser beam at the sample has been kept constant during the experiment. The experimental points have been determined by integrating the SHG part of the spectrum.

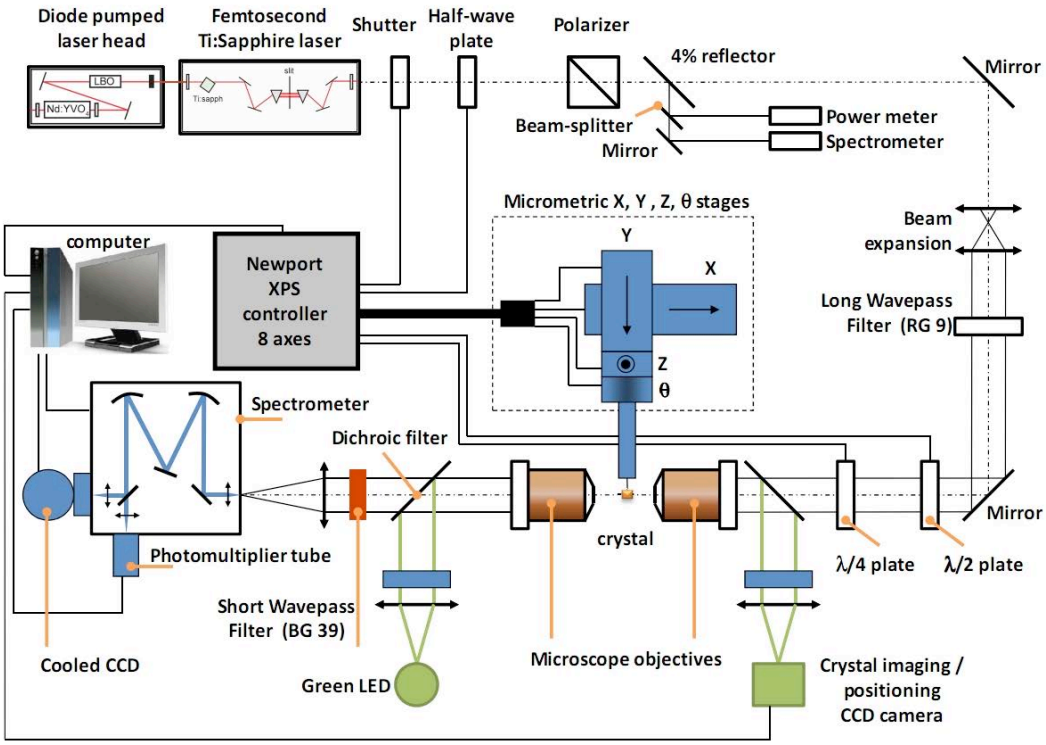

Figure S10. Schematic representation of the setup used to investigate the second harmonic generation response (SHG) of a single crystal of **1**. The 800 nm light of a

tunable Ti:Sapphire laser (670-1100 nm), providing 120 fs duration pulses with a repetition rate of 80 MHz, has been steeply focused on the sample by means of a 50x microscope objective lens, with 0.35 numerical aperture (Olympus SLMPLN50X). The crystal was mounted on a high performance X-Y-Z-φ motion controller (XPS, Newport). A second high precision rotation stage combined with a goniometric head was also fixed on this stage to allow for fine tuning of the crystal position, as well as for precise rotation of the crystal about the *b* axis. The size of the laser beam at the focal plane of the objective lens was about 1 μm, thus offering the possibility for high spatial resolution investigation of the second order nonlinear optical response. The power of the laser beam has been controlled by a combination of a λ/2 waveplate and a Glan-Taylor polarizer. A second λ/2 achromatic waveplate (700-1000nm, Edmund Optics) was placed after the polarizer in order to set the polarization of the incident laser beam on the sample. A second microscope objective lens with 25 mm working distance and 0.25 numerical aperture (Olympus SLMPLN20X) was positioned opposite to the first objective lens with its focal plane also on the crystal in order to collect the transmitted SHG light, as well as to provide for in situ, high magnification visualization of the surface of the crystal. The transmitted light has been filtered by means of a BG 39 Schott filter in order to eliminate the presence of the fundamental beam and the SHG spectra were recorded by a liquid nitrogen cooled Charge-Coupled Device camera (SPEC10, Princeton), mounted on an ACTON SP2356i Roper Scientific spectrograph.

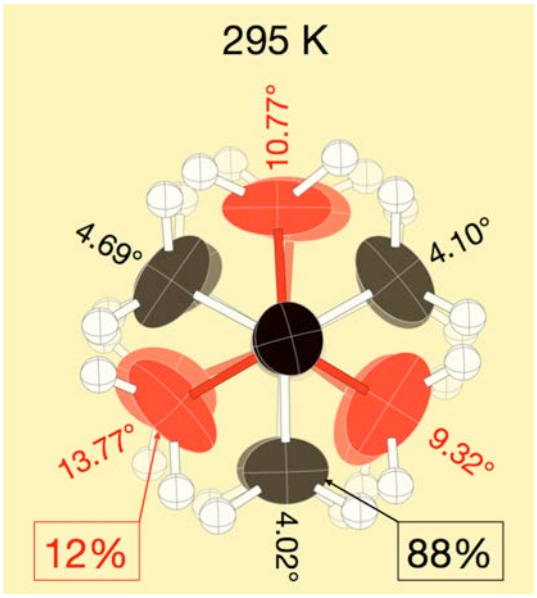

(a)

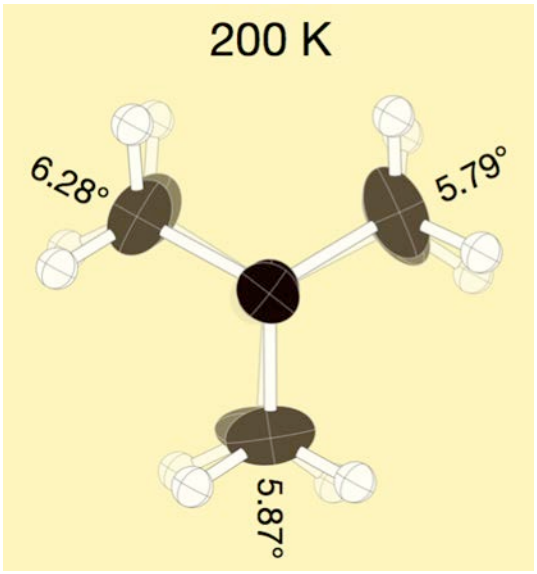

(b)

Figure S11. Dihedral angles for the three blades of the 1,4-Bis(ethynyl)bicyclo[2.2.2]octane (BCO) helical rotor in the crystal structure of **1** (with thermal ellipsoids drawn at 50% probability level). (a) At 295 K, the average dihedral angle for the (white) rotor with the larger residence site occupancy (88%) is 4.27°. The averaged value for the (red) rotor in the more constrained position with a shorter residence site occupancy (12%) is 11.29°. (b) At 200 K, the average dihedral angle for the single rotor increases up to 5.98°.

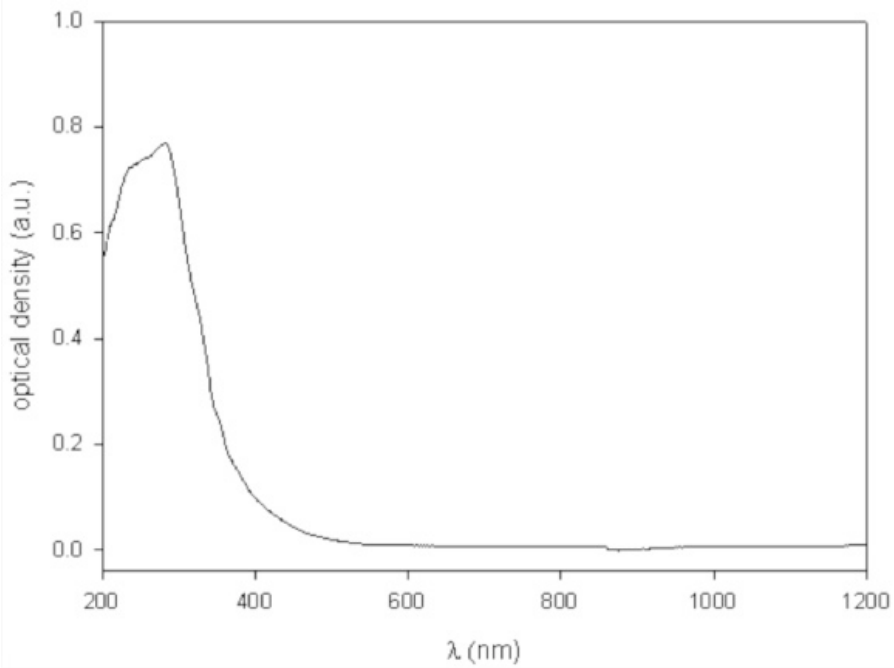

Figure S12. Electronic absorption spectra of crystals of **1** deposited on a quartz plate.

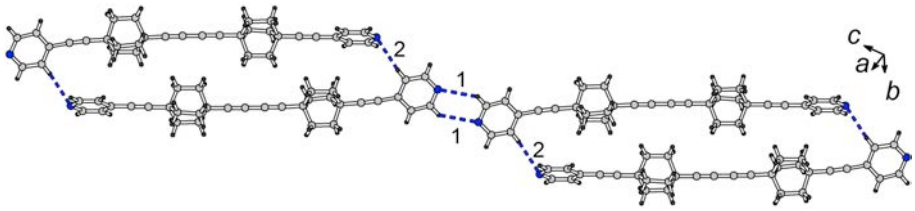

Figure S13. Geometry of the set of two C–H···N hydrogen bonds parallel and transverse to the strings available in Table S1.

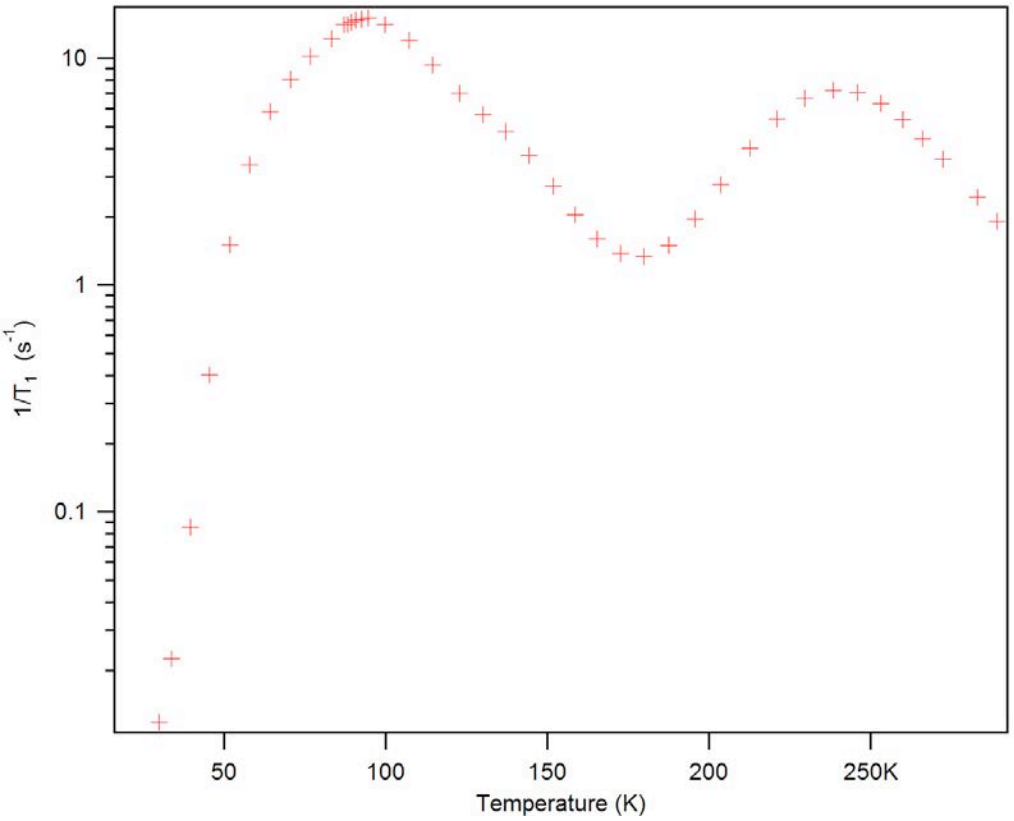

Figure S14. Variable temperature proton-spin lattice relaxation, VT ^{1}H T_1^{-1}, for 1,4-bis(3-((trimethylsilyl)ethynyl)bicyclo[1.1.1]pent-1-yl)buta-1,3-diyne, **4** at 55 MHz. Data at higher field are needed for a proper fit to the Kubo-Tomita equation, $\tau_c = \tau_0 \, exp \, (E_a/kT)$, yet the similarity with the results for **1** (Figure 2a) is already apparent. A comprehensive, compared analysis of the dynamics of **1** and **4** also requires the knowledge of the crystal structure of **4** and will be reported in due course.

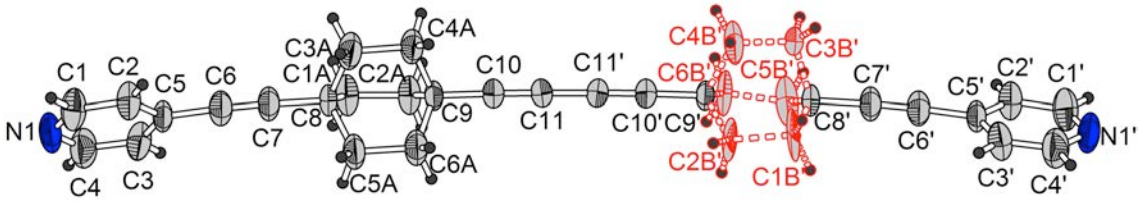

(a)

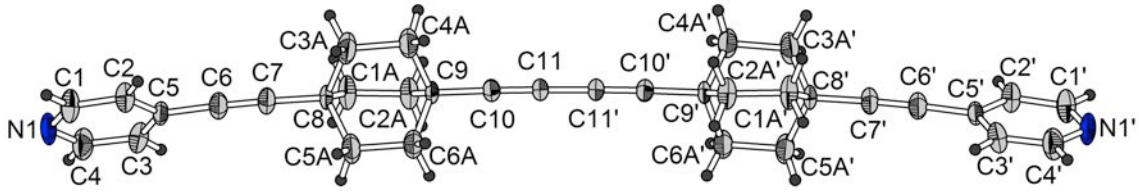

(b)

Figure S15. Structural Figure with 50% probability ellipsoids. (a) at 295 K. For clarity, only the majority (solid white lines) and minority (red dashed lines) configurations are shown for the left and right rotators, respectively. (b) at 200 K.

Table S1. Geometry of C–H···N hydrogen bonds in the structure of **1.**

Bond type*	H···N distance, Å	C···N distance, Å	C–H···N angle, º
1, 293 K	2.93	3.603(3)	130.3
1, 200 K	2.94	3.607(3)	130.2
2, 293 K	2.76	3.618(3)	154.6
2, 200 K	2.71	3.574(3)	154.3

* The two types of hydrogen bonds in **2** are shown in Figure S13

References

37. Perdew, J. P.; Burke, K.; Ernzerhof, M. *Phys. Rev. Lett.* **1997**, *78*, 1396.
38. Adamo, C.; Barone, V. *J. Chem. Phys.* **1999**, *110*, 6158.
39. Frisch, M. J.; Pople, J. A.; Binkley, J. S. *J. Chem. Phys.* **1984**, *80*, 3265.
40. Troullier, N.; Martins, J. L. *Phys. Rev. B* **1991**, *43*, 1993.
41. Nosé, S. *J. Chem. Phys.* **1984**, *81*, 511.
42. Hoover, W. G. *Phys. Rev. A* **1985**, *31*, 1695.